Electronic Supplementary Material (ESI) for Journal of Materials Chemistry A
This journal is © The Royal Society of Chemistry 2013

Supporting Information for Low Temperature Atomic Layer Deposition of Highly Photoactive Hematite Using Iron(III) Chloride and Water

Jeffrey A. Klug,[*,†] Nicholas G. Becker,[†] Shannon C. Riha,[†] Alex B. F. Martinson,[†]
Jeffrey W. Elam,[‡] Michael J. Pellin,[†] and Thomas Proslier[*,†]

Materials Science Division, Argonne National Laboratory, Argonne, Illinois 60439, USA, and
Energy Systems Division, Argonne National Laboratory, Argonne, Illinois 60439, USA

E-mail: jklug@anl.gov; prolier@anl.gov

Thermochemical Simulations

Thermochemical calculations were performed with a commercial software package[1] in order to investigate potential limitations of the $FeCl_3$ / H_2O ALD process. The vapor phase reaction of $FeCl_3$ and H_2O was compared with similar reactions involving two metal chlorides which were previously examined as ALD precursors and found to be non-ideal. **Figure S1**a shows the Gibbs free energies calculated as a function of temperature for reactions resulting in the formation of either solid Fe_2O_3 or solid FeOCl. At all temperatures from $0 - 500$ °C, ΔG for either reaction was found to be negative. However, the two $\Delta G(T)$ curves intersect near 200 °C with the Fe_2O_3

---

[*] To whom correspondence should be addressed
[†] Materials Science Division, Argonne National Laboratory, Argonne, Illinois 60439, USA
[‡] Energy Systems Division, Argonne National Laboratory, Argonne, Illinois 60439, USA

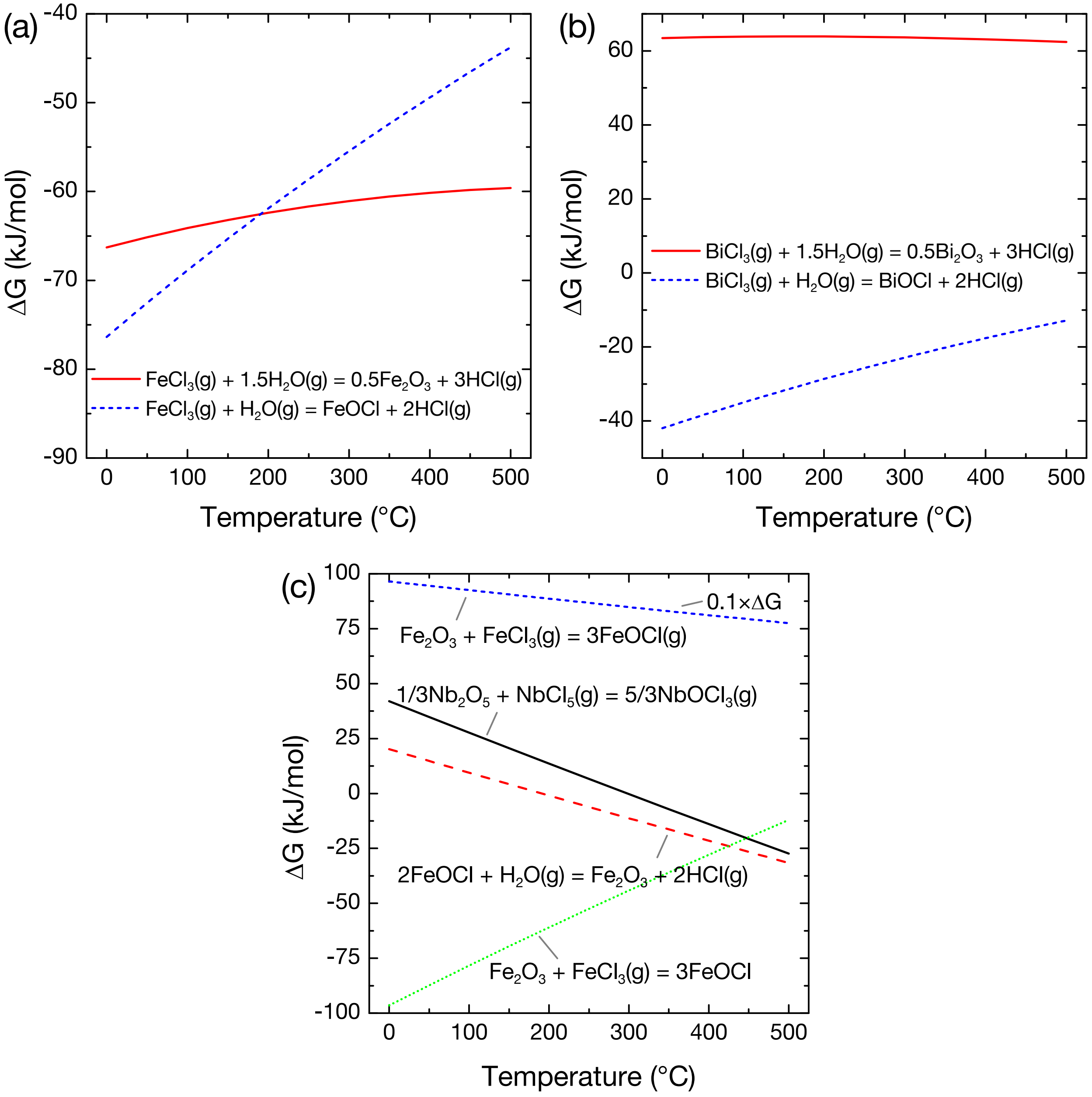

Figure S1: Thermochemical simulations of Gibbs free energies of reactions between H_2O and (a) $FeCl_3$ or (b) $BiCl_3$, and (c) comparison between etching reactions involving either $FeCl_3$ or $NbCl_5$.

reaction increasingly favored above 200 °C. In contrast, analogous calculations for another trivalent metal chloride, $BiCl_3$ (Figure S1b) found that the oxide formation reaction was unfavorable at all temperatures in the range examined. The $BiCl_3$ result is consistent with previous experimental work by Schuisky where ALD with alternating exposures to $BiCl_3$ and H_2O between 300 – 500 °C produced bismuth oxychloride films at all temperatures.[2]

Figure S1c shows a comparison of calculated ΔG for reactions involving $FeCl_3$ and $NbCl_5$. $NbCl_5$ has been observed previously to be unsuitable for ALD of Nb_2O_5 due to a self-etching effect.[3] The etching was understood to arise due to the formation of a volatile niobium oxychloride (e.g. $NbOCl_3$) as $NbCl_5$ vapor reacts with solid Nb_2O_5. The calculated Gibbs energy of such a reaction (solid black curve) is increasingly negative above 300 °C. An analogous reaction between $FeCl_3$ vapor and solid Fe_2O_3 (short-dashed blue curve) was found to be highly unfavorable with a positive ΔG exceeding 750 kJ/mol at all temperatures examined. By contrast, a negative ΔG was calculated for all temperatures assuming a solid FeOCl product (dotted green curve). This reflects the fact that FeOCl is not volatile in the temperature range examined. FeOCl is stable up to 376 °C above which it decomposes producing Fe_2O_3 and $FeCl_3$.[4] Furthermore, reaction of H_2O vapor with solid FeOCl to produce Fe_2O_3 (dashed red curve) was found to be energetically favorable above 200 °C. Consequently, any FeOCl solid produced during the $FeCl_3$ exposures for Fe_2O_3 ALD would be converted to Fe_2O_3 during the subsequent H_2O exposures.

Film Nucleation

Figure S2 shows the results of a QCM investigation of the initial nucleation of ALD Fe_2O_3 on an *in situ*-prepared Al_2O_3 surface. Immediately prior to Fe_2O_3 growth, the QCM sensor was coated with 30 cycles of ALD Al_2O_3 using trimethylaluminum (TMA) and H_2O. The mass trace (QCM signal versus time) during the first 6 $FeCl_3$ / H_2O cycles is shown in Figure S2a. The initial $FeCl_3$ dose resulted in a mass increase $\sim$ 12 ng/cm^2, roughly 20% of the steady-state $FeCl_3$ mass gain. The first H_2O exposure led to a $\sim$ 6.5 ng/cm^2 decrease in mass, resulting in a relative mass change $\sim$ 0.56 for the first ALD cycle as shown in Figure S2b. This is in good agreement with the steady-state value (0.550 ± 0.006) although given the small magnitude of mass changes during the first cycle the uncertainty in the measured $\Delta m_1/\Delta m_0$ is relatively large. While the cause of the low mass changes observed during the first ALD cycle is unclear, problems related to precursor delivery may have resulted in a sub-saturating $FeCl_3$ dose during the first cycle. The mass gain resulting from the second $FeCl_3$ exposure was observed to differ from both that of the first cycle and the steady-state Δm_0 in magnitude and transient shape. After an initial sharp mass gain, the QCM signal rose slowly to a value ~ 80 ng/cm^2 during the subsequent purge. The mass decrease following the second H_2O dose led to a relative mass gain for the second ALD cycle more than 25% larger than the average post-nucleation $\Delta m_1/\Delta m_0$. Furthermore, the net mass change during the second cycle was nearly twice the magnitude of the steady-state Δm_1. This suggests significantly more Cl is retained during cycle number 2 since $m_{\mathrm{Fe_2Cl_6}}/m_{Fe_2O_3} \sim 2$.

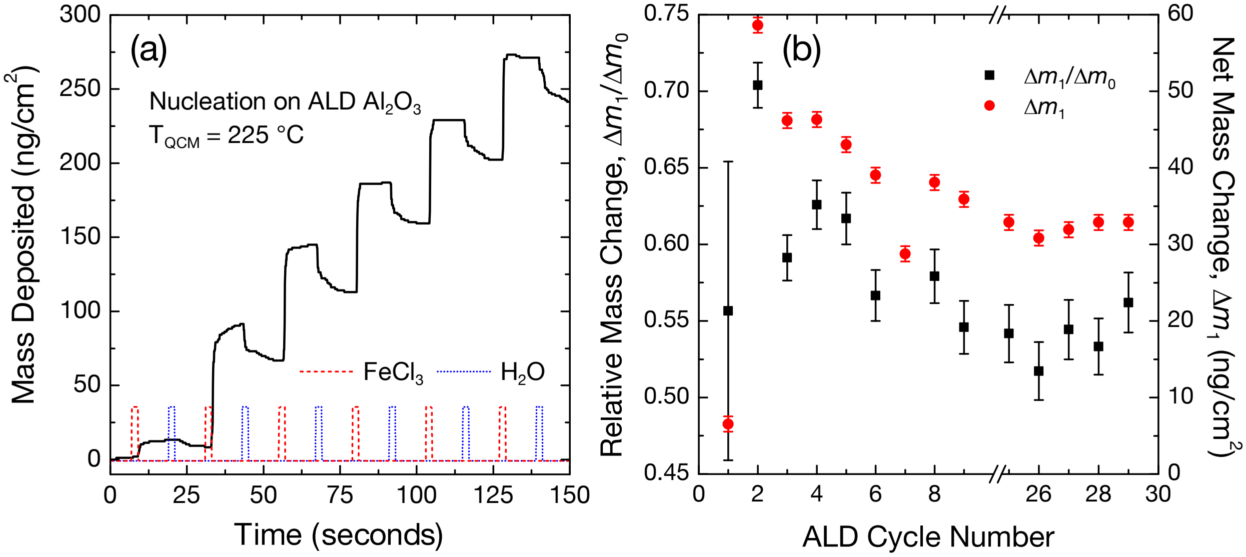

Figure S2: QCM measurement of Fe_2O_3 nucleation at 225 °C. (a) QCM mass deposited versus time and (b) relative mass change, $\Delta m_1/\Delta m_0$ (■), and net mass change, Δm_1 (●), versus ALD cycle number during initial nucleation on an *in situ*-prepared Al_2O_3 surface.

The relative and net mass gains recorded for the next 3 cycles were significantly closer to, yet still larger than 0.55 and 33 ng/cm^2, respectively. The transient shape of the QCM trace was observed to evolve over cycles 2, 3, and 4, with cycle number 4 having qualitatively the same shape observed in Figure 1a. The origin of the enhanced Fe_2O_3 growth rate during cycles $2-9$ on the ALD Al_2O_3 surface is unknown, but may result from a higher concentration of OH groups on the Al_2O_3 compared to the Fe_2O_3, or from a catalytic effect of the ALD Al_2O_3 on the ALD Fe_2O_3 surface reactions. The larger $\Delta m_1/\Delta m_0$ values during cycles $2-9$ of Fe_2O_3 ALD on the ALD Al_2O_3 surface may result from residual chlorine deposited on the Al_2O_3 that increases the

Δm_1 value. This hypothesis is supported by the RBS and XRF data presented below.

Composition

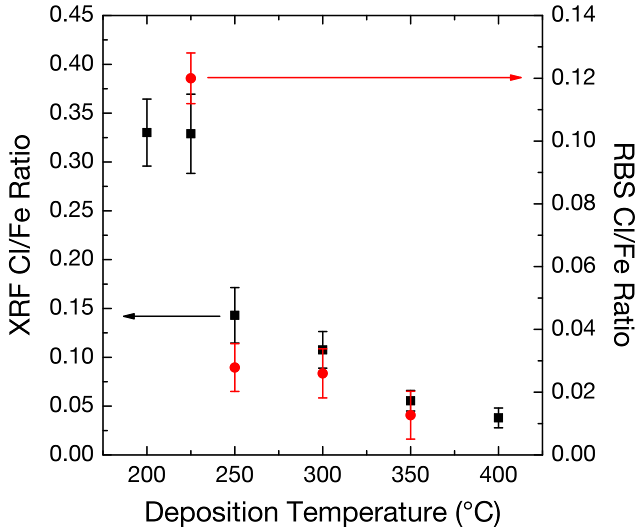

Figure S3: Film composition versus deposition temperature measured by XRF (■) and RBS (●). The XRF ratio represents the ratio between the Cl and Fe XRF peak areas and was not corrected for the difference in sensitivity factors (i.e. XRF cross section and detector efficiency) for the two fluorescence lines. That the XRF ratio differs from the absolute RBS atomic ratio by a fixed linear scaling factor confirms the equivalence of the XRF and RBS measurements. All samples were grown with 200 cycles of $FeCl_3$ and H_2O on Si(001). Films grown at 225 °C, 250 °C, and 300 °C were deposited on Al_2O_3-coated Si(001).

Figure S3 shows the deposition temperature dependence of film composition determined by RBS and XRF for a series of samples deposited with 200 cycles of $FeCl_3$ and H_2O. Comparison between the Cl/Fe ratios determined by RBS and XRF shows good agreement between the two data sets with a large decrease observed between 225 °C and 250 °C and a slower decrease with increasing deposition temperature above 250 °C. Within the uncertainties of each measurement, the XRF ratio differs from the RBS ratio by a fixed scaling factor due to the difference in XRF sensitivity for Cl Kα ($\lambda = 4.729$ Å) and Fe Kα ($\lambda = 1.937$ Å) arising from both fluorescence generation (cross section) and detection (detector efficiency). A larger temperature range was studied with XRF with characterization of films grown at 200 °C and 400 °C performed in addition to the

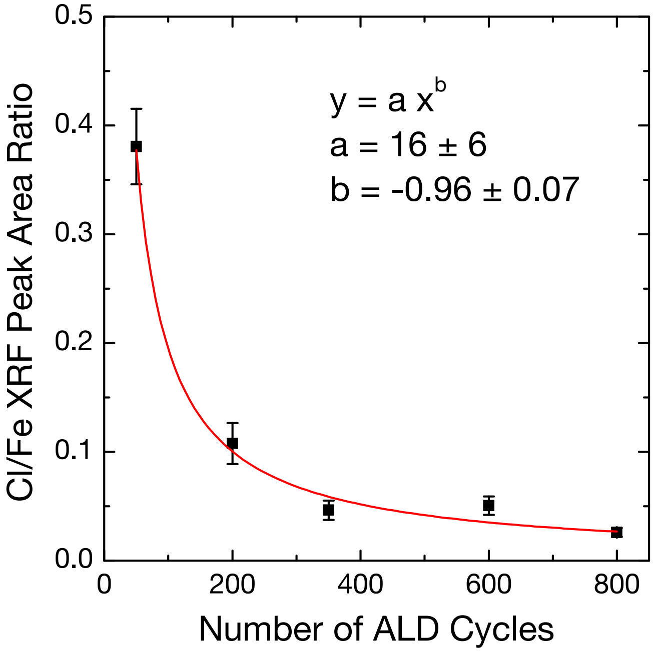

Figure S4: XRF peak area ratio Cl/Fe as a function of film thickness in number of ALD cycles. All films were deposited on Al_2O_3-coated Si(001) substrates at 250 °C.

sample set measured by RBS. At 200 °C, the relative Cl concentration, Cl/Fe was not significantly different than that of the 225 °C sample. The Cl/Fe ratio at 400 °C was slightly lower than at 350 °C, following the same trend observed between 250 – 350 °C.

Slight shifts observed in the RBS data indicated that the Cl content was likely inhomogeneous with increased concentration at or near the film-substrate interface. However, due to the small film thickness RBS depth profiling for Cl was not feasible. To examine this in more detail, a series of films deposited at 250 °C with different thicknesses were analyzed by XRF. **Figure S4** shows the thickness dependence of the relative Cl concentration, Cl/Fe. A clear decrease in Cl/Fe was observed with increasing number of ALD cycles, with the data well described by a Thickness^{-1} trend. This indicates that the majority of Cl present was deposited during the first few cycles and that increasing numbers of ALD cycles do not significantly increase the absolute Cl content. It is likely that the Cl is present as Al-Cl species formed during the initial Fe_2O_3 ALD cycles on the ALD Al_2O_3-coated substrate.[6]

Morphology

Film density, thickness, and surface roughness were characterized by analysis of XRR data from samples deposited with 50, 200, and 600 ALD cycles at temperatures between 225 – 300 °C. **Figure S5** shows a summary of the XRR analysis of films grown at 250 °C on Si(001) and fused quartz substrates. At a given deposition temperature, thickness was observed to increase linearly with number of ALD cycles, indicative of ALD growth. Film density and more so film roughness increased with increasing number of cycles. Comparison of films grown at different temperatures found a ~ 5 % lower film density and a lower growth rate ($\sim$ 0.04 nm/cycle) at 225 °C. Increased surface roughness was observed with increasing deposition temperature.

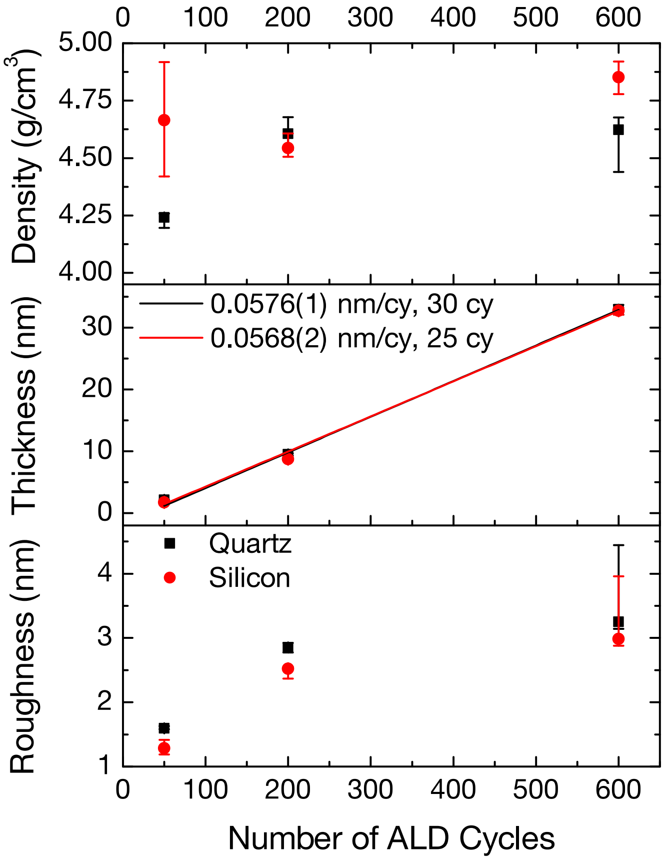

Figure S5: Summary of XRR analysis of films grown at 250 °C on Si(001) (●) and fused quartz (■) substrates. Density (top), thickness (center), and roughness (bottom) are shown as a function of number of ALD cycles.

Surface morphology was further characterized by AFM for a series of 200 cycle films deposited

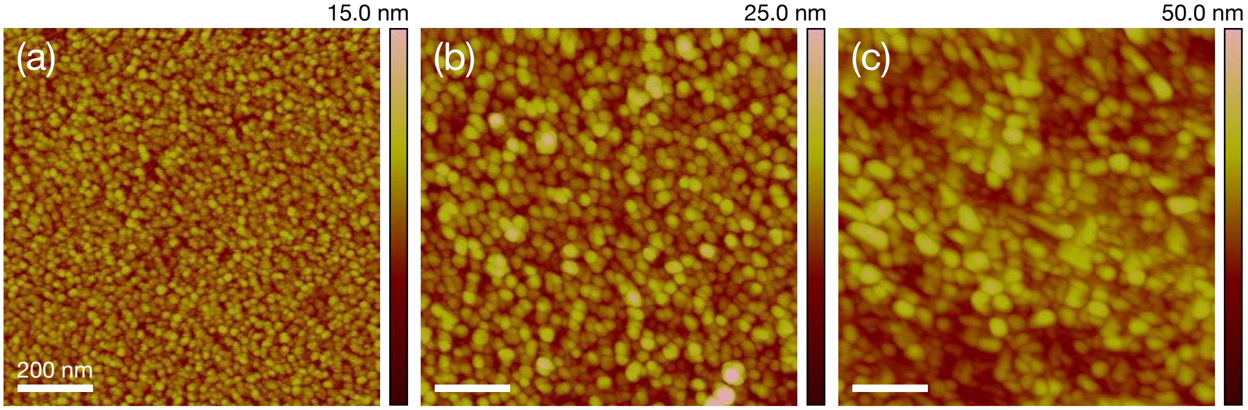

Figure S6: Evolution of film morphology with deposition temperature. AFM images of Fe_2O_3 films grown on Si(001) with 200 cycles of $FeCl_3$ and H_2O at deposition temperatures of (a) 250 °C, (b) 300 °C, and (c) 350 °C.

on Si(001) at 250 °C, 300 °C, and 350 °C. The AFM images in **Figure S6** show the evolution of film morphology with deposition temperature. A clear roughening was observed characterized by increases in both feature size and RMS roughness (RMS roughness at 250 °C, 300 °C, and 350 °C were 1.3 nm, 3.3 nm, and 4.6 nm, respectively) with increasing growth temperature.

Crystallinity

Figure S7 shows the X-ray crystallite sizes determined from GIXRD measurements of 600 cycle (~ 35 nm) films grown at 250 °C and 300 °C. The average crystallite size of an as-deposited 250 °C film was 7.3 ± 0.8 nm, while that of an as-deposited 300 °C film was 11.5 ± 0.5 nm indicating a small dependence of grain size on deposition temperature. A much larger effect was observed due to post-deposition annealing. The average crystallite size of a 300 °C film annealed at 500 °C was 29 ± 1 nm. In addition, while the values of τ determined at each momentum transfer, Q_{cen}, are scattered about $\bar{\tau}$ for the as-deposited films, a clear Q_{cen} dependence was observed for the annealed film. Peak broadening as a function of increasing Q is often associated with strain. However, in the present case strain appears to be minimal. **Figure S8**a shows that for the annealed film there is very good agreement between the measured d-spacings and those expected for bulk hematite (PDF card 33-0664). The Q-dependence was likely related to the asymmetric GIXRD measurement

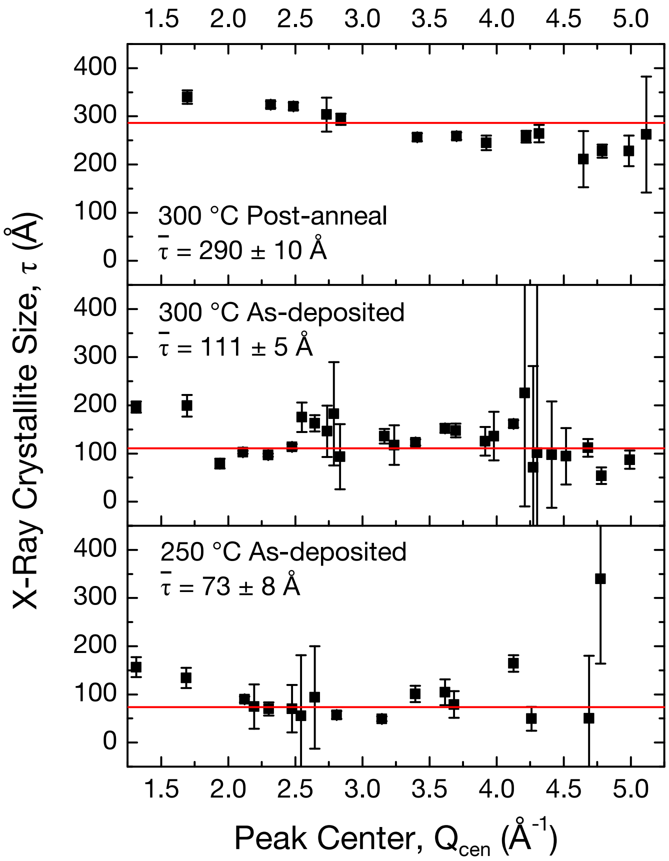

Figure S7: X-ray crystallite sizes determined from GIXRD peak widths for (top) a 500 °C annealed film grown at 300 °C, and as-deposited films grown at (center) 300 °C and (bottom) 250 °C. Each film was grown with 600 cycles ($\sim$ 35 nm) of $FeCl_3$ and H_2O on an Al_2O_3-coated silica substrate. Peak widths were determined from fits to the diffraction peaks using a pseudo-Voigt lineshape. Red horizontal lines indicate the average crystallite size, $\bar{\tau}$ for each film.

geometry.

During an asymmetric GIXRD measurement, the diffraction vector rotates with respect to the surface normal such that as the detector angle 2θ increases, the observed crystallites are oriented increasingly in plane.[5] For a given incident angle, α, the angle between the sample surface and the measured diffraction planes is $\theta - \alpha$ for a given 2θ. Therefore, for crystalline grains lacking spherical symmetry, an evolution of measured crystallite size should be observed with increasing detector angle. To estimate the asymmetry of the grain structure of the annealed film, the data was analyzed with a simplified model assuming ellipse-shaped crystallites. The data presented in

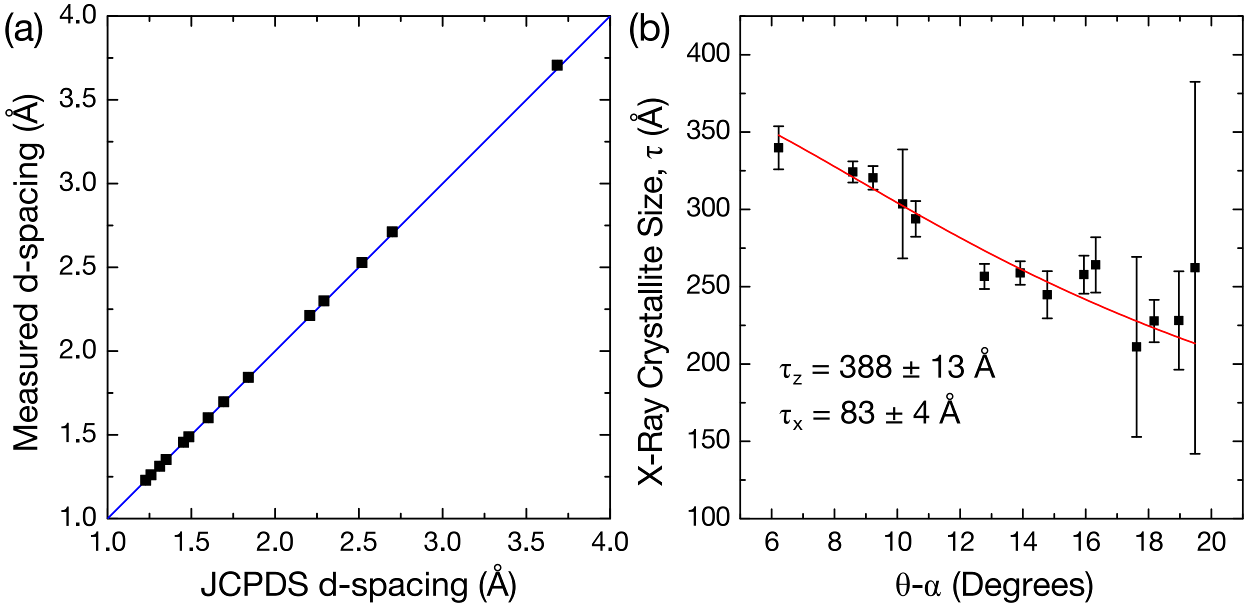

Figure S8: GIXRD analysis of annealed film. The (a) measured d-spacing is shown versus bulk d-spacing for α-Fe_2O_3. Bulk values were taken from the JCPDS database (PDF card 33-0664). The blue line shows a slope of 1 and is included as a guide to the eye. The (b) measured crystallite size is shown as a function of the angle between the diffraction planes and the sample surface, $\theta - \alpha$. The red curve is a fit to the data derived from an ellipse-shaped crystallite model.

Figure S8b was fit to a function of the form

$$\tau(\theta - \alpha) = \frac{\tau_z \tau_x}{\sqrt{\tau_x^2 \cos^2(\theta - \alpha) + \tau_z^2 \sin^2(\theta - \alpha)}} \tag{S1}$$

where τ_x and τ_z are the average crystallite size in the in-pane and out-of-plane directions, respectively. Using the elliptical model, τ_x and τ_z were determined to be 8.3 ± 0.4 nm and 39 ± 1 nm, respectively indicating significantly asymmetric crystallites. The τ_z is remarkably close to the film thickness ~ 35 nm, which suggests that while simplified, the model well approximates the actual grain structure. The large asymmetry in the crystallite size is consistent with columnar grains.

Photoelectrochemical Performance

Figure S9 shows the photocurrent density at 1.53 V vs. RHE as a function of deposition temperature for several films under 0.4 sun (annealed and as-deposited) and 1.0 sun (annealed) illumination. The 200 °C sample was prepared with 500 ALD cycles while all other films were deposited with 380 cycles. In all cases, the films deposited at 250 °C exhibited the highest photocurrents, although it should be noted that due to a reduced growth rate below 250 °C, the thickness of the 225 °C film is lower than that of the other samples. Upon annealing the current density increased for films grown above 250 °C and decreased for films grown below 250 °C. As discussed above, the improvement in current density for the high temperature films is likely due to increased crystallinity and removal of secondary phases after annealing. The reversal of influence of annealing observed near 250 °C is well correlated to the deposition temperature dependence of the Cl content (Figure S3) which abruptly increases below 250 °C. If Cl diffuses away from the film-substrate interface during annealing, there is likely a critical concentration above which the effects of Cl impurities dominate charge recombination in the film bulk. In the present case where a relatively large amount of Cl is inhomogeneously concentrated, annealing could be expected to reduce photocurrent.

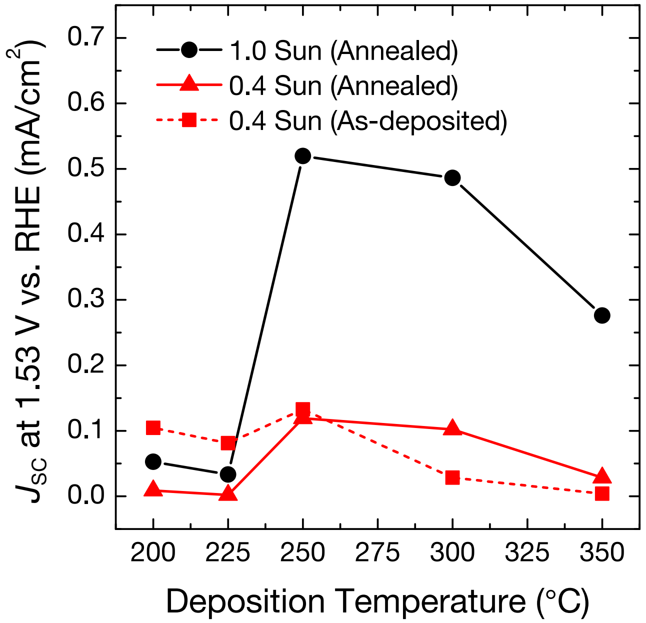

Figure S9: Photocurrent density versus deposition temperature measured at a potential of 1.53 V vs. RHE. Measurements were performed under 0.4 sun illumination for both as-deposited (▲) and annealed (■) films. The annealed samples were also characterized under 1.0 sun illumination (●). The 200 °C sample was prepared in a commercial reactor with 500 ALD cycles while all other films were deposited in our custom tool with 380 cycles.

References

(1) *HSC Chemistry*, Outokumpu Research Oy, Pori, Finland, 2001.

(2) M. Schuisky, *CVD and ALD in the Bi-Ti-O System*, Acta Universitatis Upsaliensis, Uppsala, Sweden, 2000.

(3) K.-E. Elers, M. Ritala, M. Leskelä, E. Rauhala, *Appl. Surf. Sci.* 1994, **82/83**, 468-474.

(4) Y.-D. Dai, Z. Yu, H.-B. Huang, Y. He, T. Shao, Y.-F. Hsia, *Mater. Chem. Phys.* 2003, **79**, 94-97.

(5) M. Birkholz, *Thin Film Analysis by X-Ray Scattering*, Wiley-VCH, Weinheim, 2006.

(6) L. Hiltunen, H. Kattelus, M. Leskelä, M. Mäkelä, L. Niinistö, E. Nykänen, P. Soininen, M. Tiitta, *Mater. Chem. Phys.* 1991, **28**, 379-388.